nature photonics

ARTICLES

https://doi.org/10.1038/s41566-020-00750-2

Metasurface optics for on-demand polarization transformations along the optical path

Ahmed H. Dorrah, Noah A. Rubin, Aun Zaidi, Michele Tamagnone and Federico Capasso ✉

Polarization plays a key role in science; hence its versatile manipulation is crucial. Existing polarization optics, however, can only manipulate polarization in a single transverse plane. Here we demonstrate a new class of polarizers and wave plates—based on metasurfaces—that can impart an arbitrarily chosen polarization response along the propagation direction, regardless of the incident polarization. The underlying mechanism relies on transforming an incident waveform into an ensemble of pencil-like beams with different polarization states that beat along the optical axis thereby changing the resulting polarization at will, locally, as light propagates. Remarkably, using form-birefringent metasurfaces in combination with matrix-based holography enables the desired propagation-dependent polarization response to be enacted without a priori knowledge of the incident polarization—a behaviour that would require three polarization-sensitive holograms if implemented otherwise. Our work expands the use of polarization in the design of multifunctional metasurfaces and may find application in tunable structured light, optically switchable devices and versatile light–matter interactions.

Polarization refers to the vibration of light, which is conventionally described by the trajectory of the electric field vector[1]. As a fundamental property of light, polarization has been exploited in various domains, from quantum optics and imaging to optical displays, light–matter interaction, and sensing[2–5]. Versatile manipulation of polarization and its exact characterization are therefore two crucial sought-after goals. Conventional tools for polarization control such as polarizers and wave plates consider light's polarization as a homogeneous characteristic that is managed globally. This point of view of polarization has recently been disrupted with the evolution of advanced wavefront-shaping platforms based on subwavelength-spaced arrays of optical elements (known as metasurfaces) that can manipulate light's polarization point by point across the transverse plane[6–12]. Such manipulation is commonly achieved using schemes with locally varying anisotropy, which can modify the two orthogonal polarizations of an incident waveform independently, thus converting the incident polarization state locally to any desired output[13]. These schemes have been widely exploited in versatile polarization management[12], polarization gratings[6,14,15], holography[9,16], polarization imaging[17] and in creating optical beams with structured polarization[18] (often dubbed cylindrical vector beams[19,20]), thus expanding the scope of polarization optics and its applications[21–25].

However, these new schemes and existing polarization optics share a common limitation: they consider the polarization behaviour only in a single plane transverse to the longitudinal direction, lacking the ability to control polarization over multiple planes along the propagation direction, independently, despite the advances this may bring. This elusive capability would open new paths in light's interaction with matter and biological samples, especially in vivo practices where installing multiple polarizing elements to manipulate light inside of a living tissue cannot be afforded[26]. Aside from light–matter interaction, this degree of freedom in polarization control has a direct impact on polarization characterization (known as polarimetry), which relies on projecting light onto analysers with different orientations. Reducing these into a single optical element that can project incident light onto different polarization states—to be detected along the optical path—may reveal new techniques for light's characterization. Polarizing elements of this nature are not only powerful because they combine several functionalities in a compact footprint but also due to the tunability they offer; changing the incident polarization allows the device to respond with different yet completely determined light structures that may vary in intensity and/or polarization along the optical path. Such tunability, in a sense, challenges the view of static metasurfaces and renders polarization as a powerful knob for tuning structured light longitudinally, thus enabling new technologies such as optically tunable devices and varifocal lenses. However, proposing devices of this kind immediately raises a question: light's polarization is intricately related to the photon's spin, how can such a conserved quantity change with propagation in space?

The closest answer to the question above has been provided by the digital holography community. Using spatial light modulators (SLMs), several demonstrations of optical beams with longitudinally varying states of polarization (SOP) have been reported[27–33]. The common strategy is to spatially structure the two orthogonal polarization components of an incident waveform using multiple computer-generated holograms, thereby introducing an axial (longitudinal) modulation in the SOP of the combined beam (only locally) while conserving its global energy and spin angular momentum; however, these techniques crucially assume that the incident polarization is known in advance. Notably, if the incident polarization were to change, the function of the optical set-up would be lost (see Supplementary Section 4 and ref. [34] for technical limitations). In short, a compact optical component that can impart a polarizer or wave-plate-like response along the beam's axis, regardless of the incident polarization, has remained elusive.

In this work we present a unified design strategy that enables a new class of polarizing elements which can perform an arbitrarily chosen polarization function that varies along the optical path of the beam. The underlying principle is based on spatial polarization beating, which allows an incident plane wave—after a single interaction with a nanostructured metasurface—to encounter different polarizer-like operations and/or wave-plate-like transformations

Harvard John A. Paulson School of Engineering and Applied Sciences, Harvard University, Cambridge, MA, USA. ✉e-mail: capasso@seas.harvard.edu

(only locally) at each propagation plane in space thereafter. Notably, this versatile polarization response is attained without a priori knowledge of the incident polarization and can be chosen to traverse any trajectory in polarization space, visualized on the Poincaré sphere. We envision this work to inspire new directions in polarization-switchable devices, light–matter interaction and laser micromachining in three dimensions[23,35–37].

Design concept

Our objective is to realize a polarizing element that performs different user-defined polarization operations on incident light by projecting the outcome of each function to a different output plane. The Jones matrix formalism provides a compact way to express polarization operations[38]. The transverse components of the electric field are expressed as a 2D Jones vector whereas the polarizing element is expressed as a 2×2 Jones matrix that modifies incident Jones vectors via multiplication. Hence, a longitudinally variable polarizing element (one that changes its polarization response as a function of distance) translates to a 2×2 Jones matrix that varies along the optical axis. But how can a 2×2 matrix implemented in the plane of a polarizing element modify the values of its four entries at each consecutive plane thereafter?

To answer this question, we revisit the idea of spatial harmonic beating. Figure 1a illustrates this picture: two plane waves with the same frequency and polarization, but slightly different axial propagation constants, k_z (which were realized by changing their tilt angle relative to the z-axis), undergo intensity beating in their envelope along the optical axis. If, however, we expand on this scalar picture and allow the polarization of each harmonic wave to differ, the overall polarization state of the ensemble will be modulated along the propagation direction. This is further depicted in Fig. 1b, where the same two interfering waves—now circularly polarized with opposite handedness—yield a waveform that rotates its linear polarization as it propagates. This simple picture, detailed more fully in Supplementary Section 1, is the cornerstone of a wide range of longitudinally variable polarization controls based on digital holography; however, these approaches assume that the polarization of incident light (its Jones vector) is predetermined, that is, other incident polarizations cannot be handled using the same set-up. To surmount this obstacle, we pose the following question: what if we allow these waveforms to be weighted by 2×2 Jones matrices rather than Jones vectors?[17] Mathematically, this translates to a matrix-valued ensemble in which all four matrix elements (and its two eigen vectors) undergo beating with propagation, thus creating a polarization response that changes as a function of distance. Inspired by this thought, our devices implement the following superposition

$$\tilde{U}(r,z) = \mathrm{e}^{-i\omega t}\sum_{m=-N}^{N}\tilde{A}^{(m)}J_0(k_r^{(m)}r)\mathrm{e}^{ik_z^{(m)}z}, \qquad (1)$$

where $J_0(k_r r)$ is the zeroth-order Bessel function of the first kind[39] with the time-harmonic dependence $\mathrm{e}^{-i\omega t}$, $k_r^{(m)}$ and $k_z^{(m)}$ denoting its transverse and longitudinal wavenumbers (spatial frequencies), respectively, and r is the radial distance, whereas $\tilde{A}^{(m)}$ are 2×2 matrix-valued coefficients for each of the $2N+1$ Bessel functions in the superposition (the full derivation of equation (1) can be found in Supplementary Section 2). Our choice to set the Bessel functions as the co-propagating spatial harmonics is not fundamental, but rather advantageous for two reasons: first, the Bessel function is an exact solution to the wave equation, therefore enabling a fully analytical description of our devices. Second, Bessel beams—traditionally generated from axicons—are favoured for their diffraction-resistant and self-healing nature[40], which serve our aim for constructing a longitudinally variable response over a long range. Our devices thus implement a superposition of co-propagating Bessel functions, with equal separation in k_z-space, each weighted by a different 2×2 matrix, as shown in Fig. 1c. The next task is to find the matrix-valued coefficients $\tilde{A}^{(m)}$, which can be obtained from

$$\begin{bmatrix} A_{11}^{(m)} & A_{12}^{(m)} \\ A_{21}^{(m)} & A_{22}^{(m)} \end{bmatrix} = \frac{1}{L}\int_0^L \begin{bmatrix} F_{11}(z) & F_{12}(z) \\ F_{21}(z) & F_{22}(z) \end{bmatrix} \mathrm{e}^{-ik_z^m z}\,\mathrm{d}z. \qquad (2)$$

The 2×2 matrix on the right side of equation (2)—which we will denote as $\tilde{F}(z)$—is the target z-dependent polarization function chosen by design, while L is the desired range over which $\tilde{F}(z)$ will be implemented. In essence, this equation exhibits similarity with a Fourier integral[41] (albeit matrix valued) to obtain the coefficients $\tilde{A}^{(m)}$ that are then substituted into the Fourier-like series of equation (1) to obtain $\tilde{U}(r,z)$. The matrix-valued Fourier series of equation (1) can be viewed as multidimensional generalization of the scalar method introduced in ref. [42]. By construction, $\tilde{U}(r,z=z_0)$ represents a transverse distribution of 2×2 Jones matrices which, when multiplied by an incident plane wave with Jones vector $|\mathbf{E}\rangle_{\mathrm{inc}}$ such that $|\mathbf{E}_{\mathrm{out}}(r)\rangle = \tilde{U}(r)|\mathbf{E}\rangle_{\mathrm{inc}}$, yields a valid propagating solution for the wave equation in free space—$\left(\nabla^2 - \frac{1}{c^2}\frac{\partial^2}{\partial t^2}\right)|\mathbf{E}_{\mathrm{out}}(r)\rangle = 0$—subject to the constraint $\left[k_r^{(m)}\right]^2 + \left[k_z^{(m)}\right]^2 = (k_0)^2$, $k_0 = \omega/c$. Importantly, the polarization behaviour of $|\mathbf{E}_{\mathrm{out}}\rangle$ varies as a function of distance, following the arbitrarily chosen polarization response defined by $\tilde{F}(z)$. Thus, by solving for $\tilde{U}(r,z)$ at the plane $z=0$, we obtain a device that performs variable polarization operations simultaneously at different z-planes thereafter, assuming operation in the paraxial regime, as illustrated in Fig. 1d.

To show the versatility of our approach, we will demonstrate cases in which the function $\tilde{F}(z)$ mimics the behaviour of longitudinally tunable polarizers and wave plates located along the propagation direction, such that an observer—at a given point along the z-axis—would observe light that had been modified from polarization incident on the device in a way that corresponds with the desired Jones matrix $\tilde{F}(z)$. We choose polarizers and wave plates here as any complex polarization operation can be decomposed into a polarizer-like operation and a wave-plate-like transformation by the matrix polar decomposition[1]. However, the 2×2 Jones matrix distribution, $\tilde{U}$, which defines our polarizing devices is thus far only a mathematical description. In what follows, we discuss how it can be physically implemented using metasurface optics.

Results

Metasurfaces. To impart the desired polarization response $\tilde{F}(z)$ on an incident plane wave, we require an optical element that can, point by point, implement the desired Jones matrix function $\tilde{U}(r,z=0)$. Metasurfaces are a particularly convenient platform for this purpose[43]. Composed of dielectric nanopillars with structured birefringence, metasurfaces can be locally represented by a spatial arrangement of linearly birefringent wave-plate-like elements, described in Cartesian coordinates by the Jones matrix[1]

$$\tilde{J}(x,y) = R(-\phi(x,y))\begin{bmatrix} \mathrm{e}^{i\theta_x(x,y)} & 0 \\ 0 & \mathrm{e}^{i\theta_y(x,y)} \end{bmatrix} R(\phi(x,y)). \qquad (3)$$

Here, $x = r\cos(\phi)$ and $y = r\sin(\phi)$, as defined in Fig. 1, and $R(\phi)$ is the 2×2 rotation matrix.

We employ metasurfaces with rectangular dielectric nanofins (pillars) of titanium dioxide on glass, which have a higher refractive index than air[44], as exhibited in Fig. 2b. Unit cells of this topology support two propagating modes that experience different effective refractive indices (phase delays) due to anisotropy. Notably, the phase retardation values θ_x and θ_y in equation (3) are readily tuned

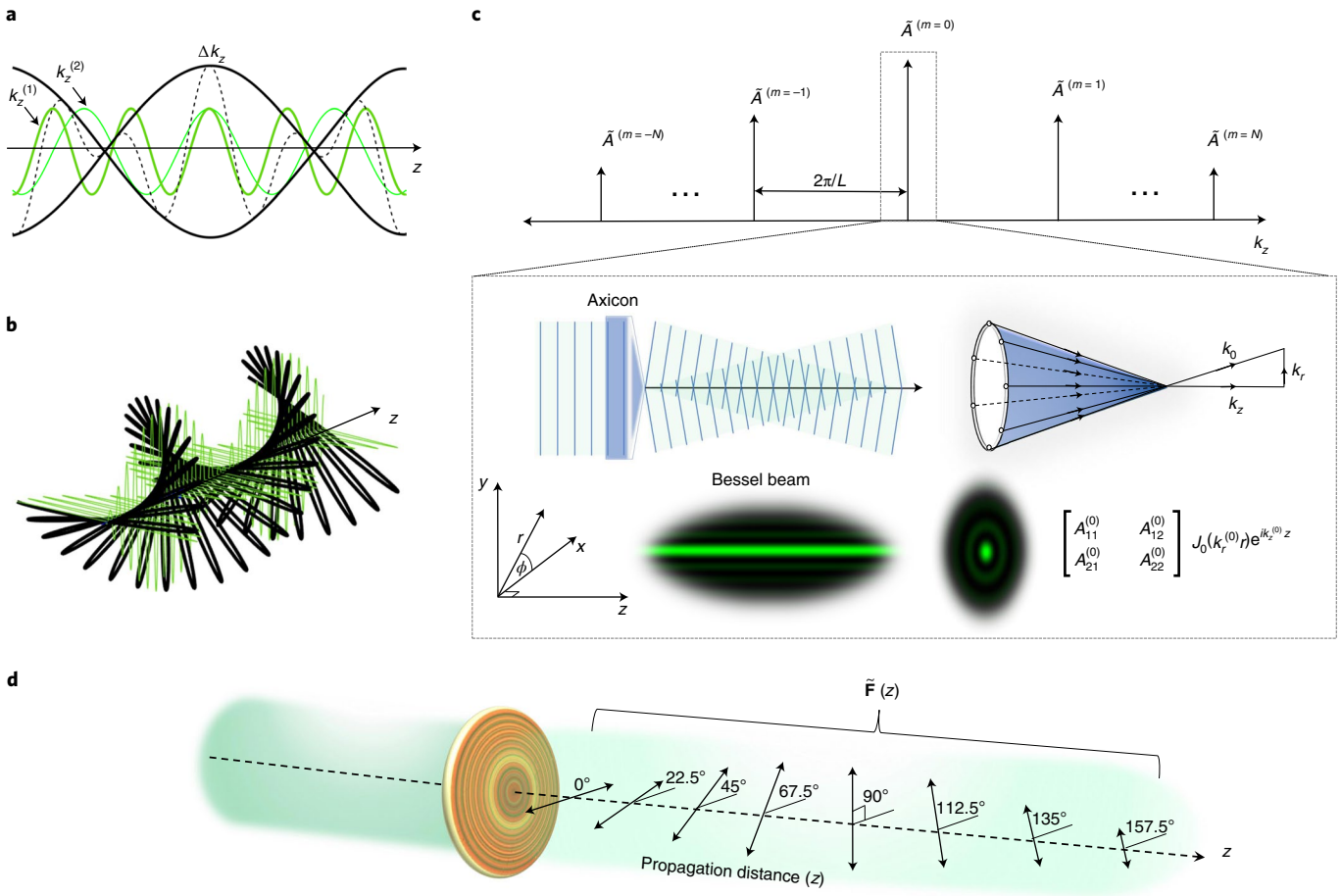

Fig. 1 | The concept of longitudinally variable polarization elements. a, Intensity beating between two scalar monochromatic plane waves (green) with the same frequency but slightly different propagation constants $k_z^{(1)}$ and $k_z^{(2)}$ produces amplitude modulation in the resulting waveform (dashed black curve) and its envelope (solid black curve); we denote this as the scalar case. **b**, The polarization beating (vector case) produced by two interfering vector waves with the same frequency, but different k_z and polarization. Here the two interfering waveforms are circularly polarized with opposite handedness, leading to a linearly polarized waveform (black) that rotates its polarization with propagation. The green curves are the orthogonal components of the black waveform projected on the vertical and horizontal planes. **c**, The design principle (matrix approach): the polarizing device implements a superposition of $2N+1$ Bessel functions with equal separation of $2\pi/L$ in k_z-space. The inset depicts a Bessel beam generated by an axicon and its decomposition into plane waves whose wavevectors lie on the surface of a cone. Each Bessel function in the sum has a slightly different cone angle and is weighted by a 2×2 Jones matrix, $\tilde{A}^{(m)}$. **d**, A schematic of a z-dependent polarizing device (polarizer or retarder), given by $\tilde{U}(r, z=0)$, which enables variable polarization operations $\tilde{F}(z)$ to be performed at different z-planes along the optical path, simultaneously. The black arrows depict the virtual principal axis orientation of the polarizing element at each z-plane.

by varying the dimensions of the nanopillars in the transverse (that is, xy) plane, whereas the physical rotational angle ϕ—which defines the anisotropy axis—can be adjusted by changing the pillar's angular orientation (about the longitudinal axis), as is now standard in a wide range of metasurfaces[9,10]. Combining linear structural birefringence with the angular rotation of the nanopillars enables the conversion of any incident vector state to another, locally, while achieving full 2π phase coverage[9]. The acquired phase shift consists of a dynamic factor due to propagation along the nanopillars and a geometric (Berry) phase factor[45] that accompanies the polarization transformation introduced by the nanopillar wave-plate-like retardance. The output phase profile and transmission response introduced by each nanopillar, as a function of its dimensions, can be found in Supplementary Section 3. For each unit cell in the designed metasurface, the nanopillar that yields the closest rendition of $\tilde{U}(r, z=0)$, while ensuring uniform transmission, is selected.

Constraints of metasurface platform. The Jones matrix so realized by our metasurface platform is everywhere subject to two important constraints. First, as suggested by equation (3), $\tilde{J}(x, y)$ locally takes the form of unitary matrices, preserving inner products, such that $\tilde{J}^{\dagger}\tilde{J} = \mathbb{I}$ (where † denotes the conjugate transpose and $\mathbb{I}$ is the 2×2 identity matrix). This is a direct consequence of the lossless nature of wave plates (the unit cells comprising the metasurface), which merely modify the relative phases of an incident waveform with no diattenuation (that is, the difference between absorption of light polarized parallel and perpendicular to an orientation axis; a diattenuating material will absorb linear polarization along one axis preferentially). Second, $\tilde{J}(x, y)$ must be symmetric, $\tilde{J}(x, y) = \tilde{J}(x, y)^{T}$, where T denotes a matrix transpose—a direct manifestation of its linear structural birefringence. These constraints limit the possible polarization behaviours that can be realized; for instance, unitarity prohibits realizing a device that introduces diattenuation to an incident waveform (such as, for example, a polarizer), whereas matrix symmetry implies that, even were a polarizer-like element to be realized, it could only analyse the complex conjugate of its intended Jones vector[9]. These constraints can be mitigated using complex configurations such as cascaded and chiral metasurfaces[46],

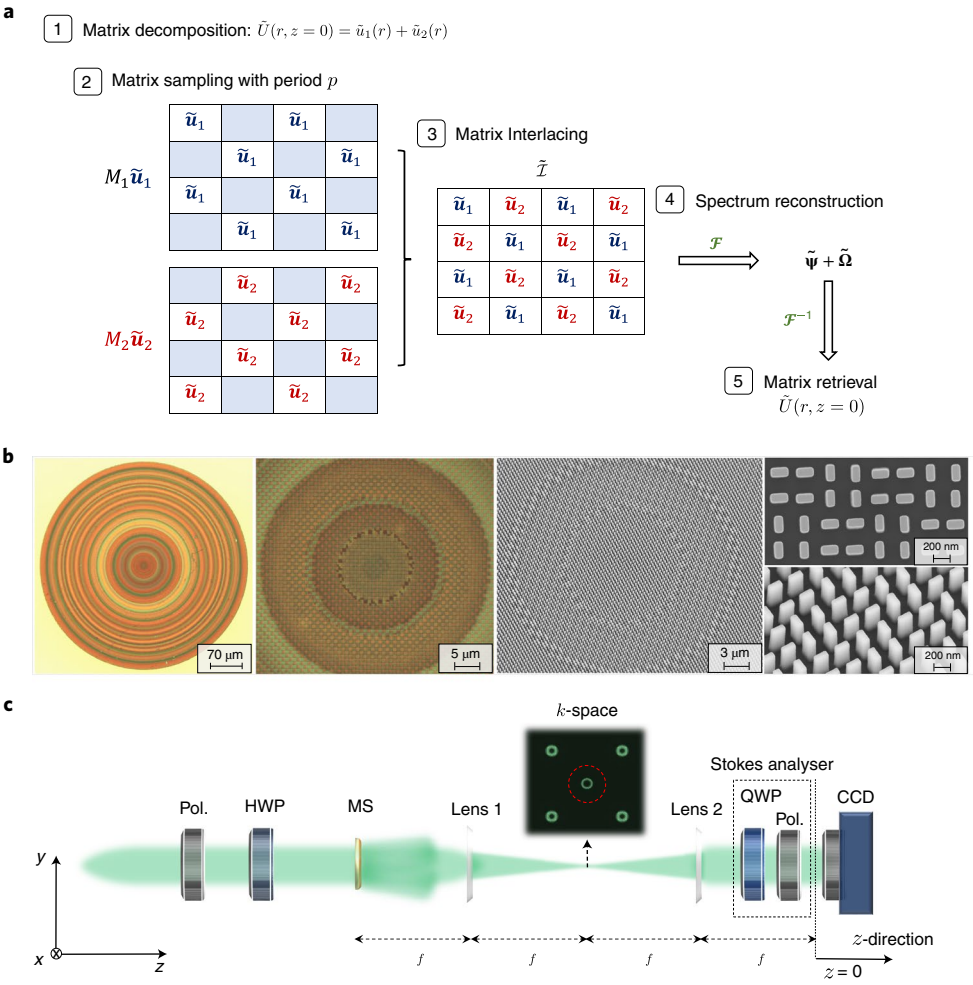

Fig. 2 | Device implementation and characterization. a, Dual matrix holography: an arbitrary symmetric matrix $\tilde{U}(r, z=0)$ may be decomposed into $\tilde{u}_1(r)$ and $\tilde{u}_2(r)$, which are then sampled and interlaced on a single metasurface. The desired Fourier spectrum of the metasurface is reconstructed via Fourier transform and filtering. The desired matrix $\tilde{U}$ is then retrieved via an inverse Fourier operation. **b**, Optical microscope and SEM images of the fabricated *z*-dependent polarizer, enabled by a metasurface consisting of TiO_2 on glass substrate. **c**, The experimental set-up, in which a 532 nm linearly polarized and collimated beam, whose polarization can be rotated with a half-wave plate (HWP), is incident on the metasurface (MS) element. A 4*f* imaging system (*f* being the focal distance of each lens) is used to reconstruct the desired Fourier spectrum, filter it and retrieve it back to real space. The full spectrum is reconstructed in the focal plane of lens 1 (as shown in the inset). Only the desired on-axis spectrum (circled in red) is transformed back to real space via lens 2, whereas the higher diffraction orders are naturally filtered away due to their large angle. The transverse beam's profile is measured along *z* using a CCD mounted on a translation stage. At each *z*-plane, the polarization is measured by performing Stokes polarimetry using a polarizer (pol.) and QWP (quarter-wave plate).

which usually suffer from further implementation challenges. We will instead introduce a unit cell multiplexing technique, inspired by holography, that enables the realization of arbitrary Jones matrices using a single unitary (lossless) metasurface, thus surmounting the first constraint. This solution is still bound to matrix symmetry, but as our aim here is to demonstrate polarizers and wave plates, with strictly linear eigen-polarizations whose Jones matrices are symmetric by construction, the second condition will always be satisfied.

Dual matrix holography. The use of lossless, phase-only platforms to holographically encode both amplitude and phase information has been considered for decades, with phase retrieval algorithms[47] and dual-phase holography[48,49] being two examples of techniques proposed for this task. The latter expresses a normalized complex scalar field as the sum of two phase-only distributions. By spatially interlacing these two phase distributions in the same plane while fulfilling the Nyquist sampling criterion, the Fourier spectrum of a complex field can be fully reconstructed if it is a band-limited signal[49]. Here we generalize this concept to apply to Jones matrix quantities by introducing a multidimensional matrix reconstruction technique termed dual matrix holography, in which a distribution of 2×2 arbitrary (unitary and/or Hermitian) matrices can be implemented using a strictly unitary platform (a Hermitian matrix is one that does not preserve inner products, its eigenvalues are real and hence it can modify the amplitude of a complex vector; more details can be found in Supplementary Section 7). This enables the realization of polarizing elements that not only enact retardance but diattenuation as well. In particular, we follow the method from ref. [49], generalizing its result to the case of matrix-valued quantities.

The above technique permits us to express an arbitrary matrix, whose eigenvalues are of mixed amplitude and phase, as a sum of two unitary matrices, whose eigenvalues are phase-only quantities. This can be repeated at every point across the spatial extent of $\tilde{U}$, forming the target metasurface profile. Figure 2a summarizes this procedure (which is fully detailed in the Methods) by which the original matrix distribution $\tilde{U}(r, z=0)$ is normalized and

decomposed into two spatially varying unitary matrices $\tilde{u}_1$ and $\tilde{u}_2$. These two new matrix distributions are then periodically sampled via complementary draughts board patterns, M_1 and M_2, following Nyquist's criterion, and then interlaced onto a single mask, denoted as $\tilde{\mathcal{I}}$. Sampling above the Nyquist criterion permits the complex Fourier spectrum of the original matrix $\tilde{U}$ to be fully reconstructed in the far field via a Fourier operation, implemented by a lens (lens 1 in Fig. 2c). Here the Fourier spectra of $\tilde{u}_1$ and $\tilde{u}_2$ are denoted by $\tilde{\mathbf{\Psi}}$ and $\tilde{\mathbf{\Omega}}$, respectively. Note that multiple copies of these spectra are generated at the Fourier plane, as shown in inset of Fig. 2c; these higher diffraction orders—the principal tradeoff for the freedom afforded by this method—can be spatially filtered. Finally, through an inverse Fourier operation performed by a second lens (lens 2 in Fig. 2c), the complex (amplitude and phase) distribution of $\tilde{U}(r, z=0)$ in real space can be fully retrieved.

Metasurface design, fabrication and testing. The matrix $\tilde{\mathcal{I}}(r,\phi)$, obtained by performing this dual-phase holography technique on the matrix $\tilde{U}$, is of the correct form for implementation by a metasurface (see equation (3)). A library of metasurface unit cells, comprising rectangular dielectric nanopillars of high refractive index (TiO_2), is constructed by varying the pillar dimensions (d_x and d_y) and their angular orientation (see Methods). For each transverse location on the metasurface, $\tilde{\mathcal{I}}(r,\phi)$ is realized by selecting its closest pillar geometry from a library, as detailed in Supplementary Section 3. The devices were fabricated via e-beam lithography and atomic layer deposition following the now-standard procedure[44] outlined in the Methods. A micrograph, as well as SEM images of a device implementing z-dependent linear polarizer, are shown in Fig. 2b, where the draughts board signature of our interlaced dual matrix implementation is observed. Here, each draughts board cell comprises four nanopillars; a closer view of the device verifies the smooth sidewall profile of these nanopillars.

All devices have been tested using the 4f system depicted in Fig. 2c, in which a 532 nm collimated polarized Gaussian beam illuminates the metasurface, generating the desired spectrum at its Fourier plane, which is then filtered and transformed back to real space via a second lens before being recorded by a charge-coupled device (CCD) camera on a translation stage (see Methods). To characterize the polarization behaviour of the output beam at each z-plane, we performed polarization measurements based on Stokes polarimetry[1]. This enabled the determination of the full, four-component polarization Stokes vector, $\overrightarrow{\mathbf{S}} = (S_0, S_1, S_2, S_3)^T$, which quantifies the shape and orientation of the polarization ellipse at each point as well as the beam's intensity and degree of polarization.

Experimental results. Several devices have been fabricated and tested; these include a polarizer, a HWP and a QWP, all with an orientation that rotates as a function of the propagation distance z. All devices have a diameter of 462 μm. Design considerations related to the device dimensions, number of Bessel beams in the superposition of equation (1), and their spatial frequencies are discussed in the Methods and fully detailed in Supplementary Section 6. In what follows, we characterize the performance of the polarizing devices. Furthermore, in Supplementary Section 5 we provide more physical insight on how these devices work in terms of energy and momentum exchange between the outer and inner parts of the beam.

Linear polarizer. We start by demonstrating a longitudinally variable linear analyser whose transmission axis is designed to virtually rotate by an angle ϕ (with respect to the x-axis) as a function of z, following the relation $\phi_z = [(z-2.5)/3]\frac{\pi}{2}$ over the space interval (2 mm ≤ z ≤ 6 mm). This polarizing metasurface modifies its diattenuation response spatially, serving as an analyser for different polarization states in parallel at each z-plane thereafter. The states of polarization being analysed vary continuously from $\hat{x}$ (0°) to $\hat{y}$ (90°) within the region z = 2.5 mm to z = 5.5 mm. Figure 3a illustrates the analyser's response. Under x-polarized incident illumination, the on-axis intensity decays gradually while propagating away from the device until it is nearly quenched at z = 5.2 mm. This is in accordance with the z-analyser's virtual transmission axis, as depicted by the red arrows, and Malus's law. By contrast, under $\hat{y}$ illumination, the on-axis intensity increases over the same space region. The extinction ratio between the two is on the order of −20 dB. Note that as the polarizing metasurface is comprised of unitary (lossless) wave-plate-like unit cells, the loss mechanism here relies on the judicious interference among the propagating modes. The polarizing effect is enacted here only locally on the non-diffracting centre spot of the beam through a deliberate exchange of energy between the beam's central spot and its outer rings. The energy of the beam is globally conserved at each z-plane. Detailed calculations for the evolution of local and global energy can be found in Supplementary Section 5.

To confirm the variable analyser action, the intensity profile has been recorded at each plane along z under different incident linear polarizations and circular polarization (see Fig. 3b–j; error bar characterization of the device can be found in Supplementary Section 8). It is observed that the (local) centroid of the beam is gradually shifted along z (away from the reference) in response to rotating the incident polarization, following the projection of the incident polarization (black arrow) onto the variable analyser axis (red arrows). The spatially non-uniform intensity along z in the case of circular polarization (Fig. 3j) is due to the finite number of Bessel terms in the superposition of equation (1) and agrees with the theoretical calculation. A more flat response could be achieved by readjusting the number of terms in the Fourier superposition. Notably, the beams generated from our device are characterized by a Bessel-like transverse profile, as depicted in Fig. 3k. The side lobes play a critical role ensuring that the polarization-tunable behaviour occurs over long propagation distances, while maintaining the finite energy of the beam, and experiencing minimal diffraction effects, as shown in Fig. 3l. In addition to tailoring diattenuation along the z-direction, our approach can be applied to engineer retardance, as discussed next.

HWP. We demonstrate a HWP with a longitudinally variable response by designing the principal axis (that is, fast axis) to locally rotate by an angle ϕ with respect to the x-axis as a function of z, following the relation $\phi_z = [(z-2.5)/3]\frac{\pi}{2}$ over the space interval (2 mm ≤ z ≤ 6 mm). In essence, this retarder rotates the polarization state of an incident linear polarization, continuously, by a total amount of 180° over the region z = 2.5–5.5 mm, preserving the linear polarization without introducing any chirality. An optical image of the fabricated device is shown in Fig. 4a where the underlying dual matrix holography implementation is signified by the draughts board pattern. Figure 4b shows the simulated longitudinal intensity profile of the output beam, assuming $\hat{x}$ incident polarization.

To characterize the polarization behaviour, full Stokes polarimetry is performed by inserting a polarizer and a QWP before the CCD to measure the polarization of light at each pixel. Figure 4c depicts the state of polarization plotted on top of the transverse intensity of the output beam, measured at different z-planes. Here, the incident plane wave is x-polarized. The polarization state evolves (locally) at the non-diffracting central spot of the beam in accordance with the spatially rotating virtual axis of the retarder along z. The detected spatial resolution of the polarization state is limited by the CCD. The on-axis intensity of our Stokes measurements is shown in Fig. 4d–f when the output analyser was oriented at 0°, 45° and 90°, and is plotted in Fig. 4g for when the analyser and QWP were oriented at 45° and 0°, respectively, to analyse for RCP. We denote these on-axis intensities as $I_{0°}$, $I_{45°}$, $I_{90°}$ and I_{RCP} (where RCP is right-hand circular polarization). At z = 2.5 mm, $I_{0°}$ is a maximum, $I_{90°}$ is a minimum and both $I_{45°}$ and I_{RCP} are at a midpoint—a signature of an

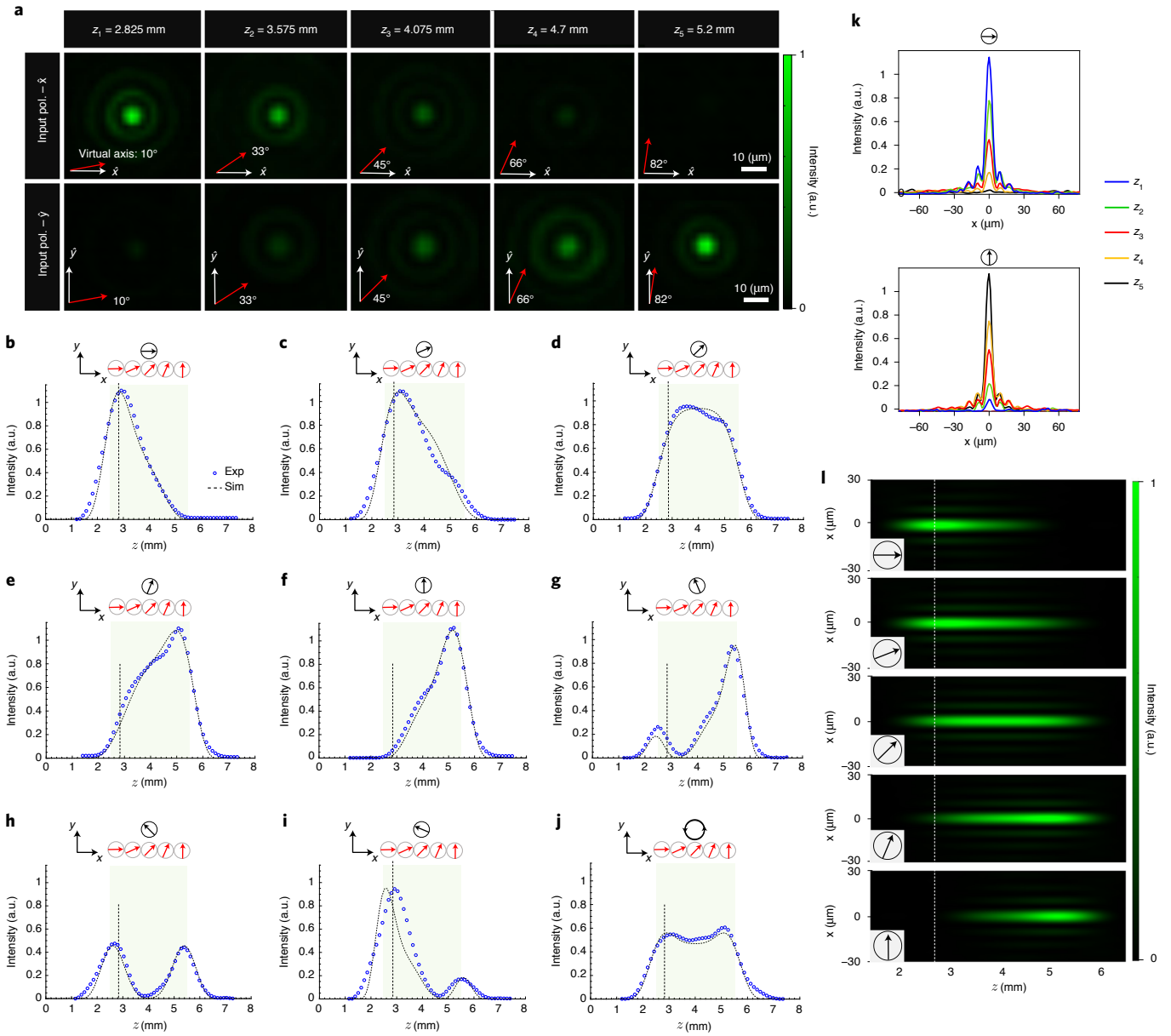

Fig. 3 | Longitudinally variable analyser. a, Measured transverse profiles of the output beam at different planes along the propagation direction for $\hat{x}$ and $\hat{y}$ incident polarizations. The white arrows depict the incident polarization (in the *xy* plane) whereas the red arrows represent the state of polarization being analysed with our device at each *z*-plane. **b**–**j**, Measured and simulated on-axis intensity as a function of *z* under different incident polarizations, namely 0° (**b**), 22.5° (**c**), 45° (**d**), 67.5° (**e**), 90° (**f**), 112.5° (**g**), 135° (**h**), 157.5° (**i**), with respect to the *x*-axis, and circular polarization (**j**). The red arrows depict the virtually varying orientations of the transmission axis of the metasurface polarizing element at five different *z*-planes, the black arrows represent the input polarization, and the vertical black dashed lines serve as a reference. **k**, Transverse intensity cross-sections for the output beam at the five *z*-planes in **a**. **l**, Longitudinal profiles of the generated pencil-like beam for each incident polarization depicted in the inset. The centroid of the on-axis intensity distribution continuously shifts away from the source in response to rotating the input polarization from 0° to 90°.

x-polarized beam. This behaviour is repeated at $z = 5.5$ mm, suggesting a return to the same polarization. However, at a propagation distance in-between ($z = 4$ mm, for instance), I_{0° is a minimum, I_{90° is a maximum and I_{45° and I_{RCP} settle at a midpoint—a signature of the orthogonal ($\hat{y}$) polarization.

To track the evolution of the output polarization state, we obtained the Stokes parameters based on these four intensity measurements at each *z*-plane: $S_0 = I_{0^\circ} + I_{90^\circ}$, $S_1 = I_{0^\circ} - I_{90^\circ}$, $S_2 = 2(I_{45^\circ}) - (I_{0^\circ} + I_{90^\circ})$ and $S_3 = 2(I_{\mathrm{RCP}}) - (I_{0^\circ} + I_{90^\circ})$ (ref. [1]; error bar plots of our Stokes measurements can be found in Supplementary Section 8). The Stokes trajectory on the Poincaré sphere, which visualizes all states of polarization expressed in terms of the Stokes vectors $(S_1,S_2,S_3)^T$, is depicted in Fig. 4h–j as a function of *z*. The trajectory has been measured under three different incident polarizations: 0°, 45° and 135°. From Fig. 4h–j, it is confirmed that the polarization state follows one complete revolution around the equator of the Poincaré sphere, which plays host to all linear polarizations. The start and end points of the closed path (marked by the red stars) are defined by the incident polarization, implying that the polarization response is maintained regardless of the incident polarization. In each scenario, the energy associated with the *x* and *y* components of the field is independently conserved, as discussed in Supplementary Section 5.

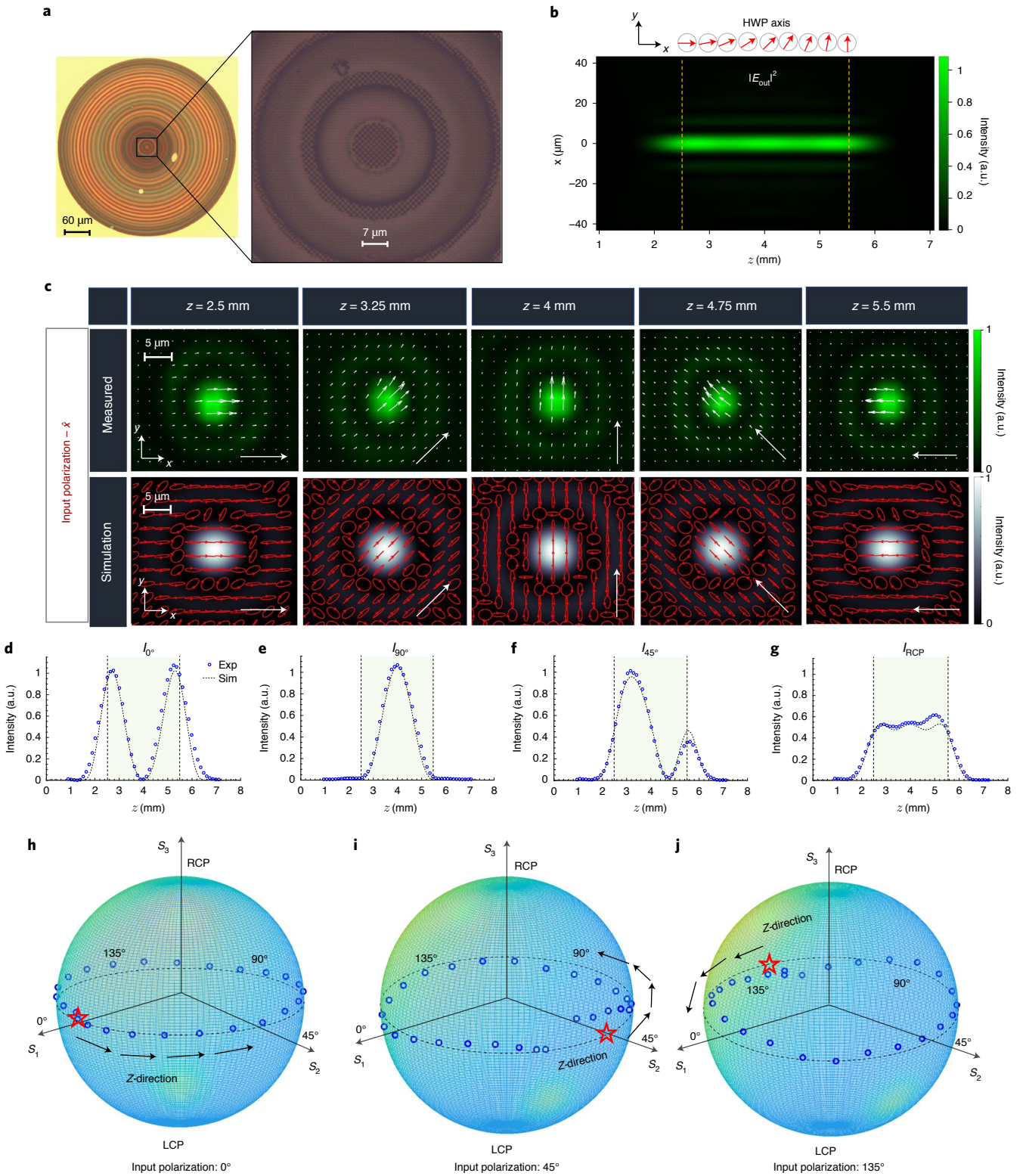

Fig. 4 | *z*-Dependent HWP. a, Optical microscope images of the fabricated device. The draughts board pattern signifies the underlying dual matrix holography implementation. **b**, A simulated longitudinal intensity profile of the output beam under *x*-polarized illumination. The red arrows depict the orientation of the fast axis at different planes along *z*, whereas the vertical dashed lines mark the region of space over which the metasurface retarder element rotates its fast axis virtually from 0° to 90°. **c**, Measured and simulated transverse intensity profiles at different *z*-planes. The state of polarization, obtained from Stokes polarimetry, is depicted by the arrows. **d**–**f**, Measured and simulated on-axis intensity profiles as a function of *z* when the output analyser's axis is oriented at 0° (**d**), 90° (**e**) and 45° (**f**), without the QWP. **g**, Measured and simulated on-axis intensity profiles as a function of *z* when the axes of the output QWP and analyser (before the CCD) are oriented at 0° and 45°, respectively, to analyse for RCP. **h**–**j**, The Stokes trajectory (based on the measurements in **d**–**g**) evolves on the equator of the Poincare sphere as a function of *z* under three different incident polarizations: 0° (**h**), 45° (**i**) and 135° (**j**), confirming the continuous rotation in the state of polarization for each case. LCP, left-hand circular polarization.

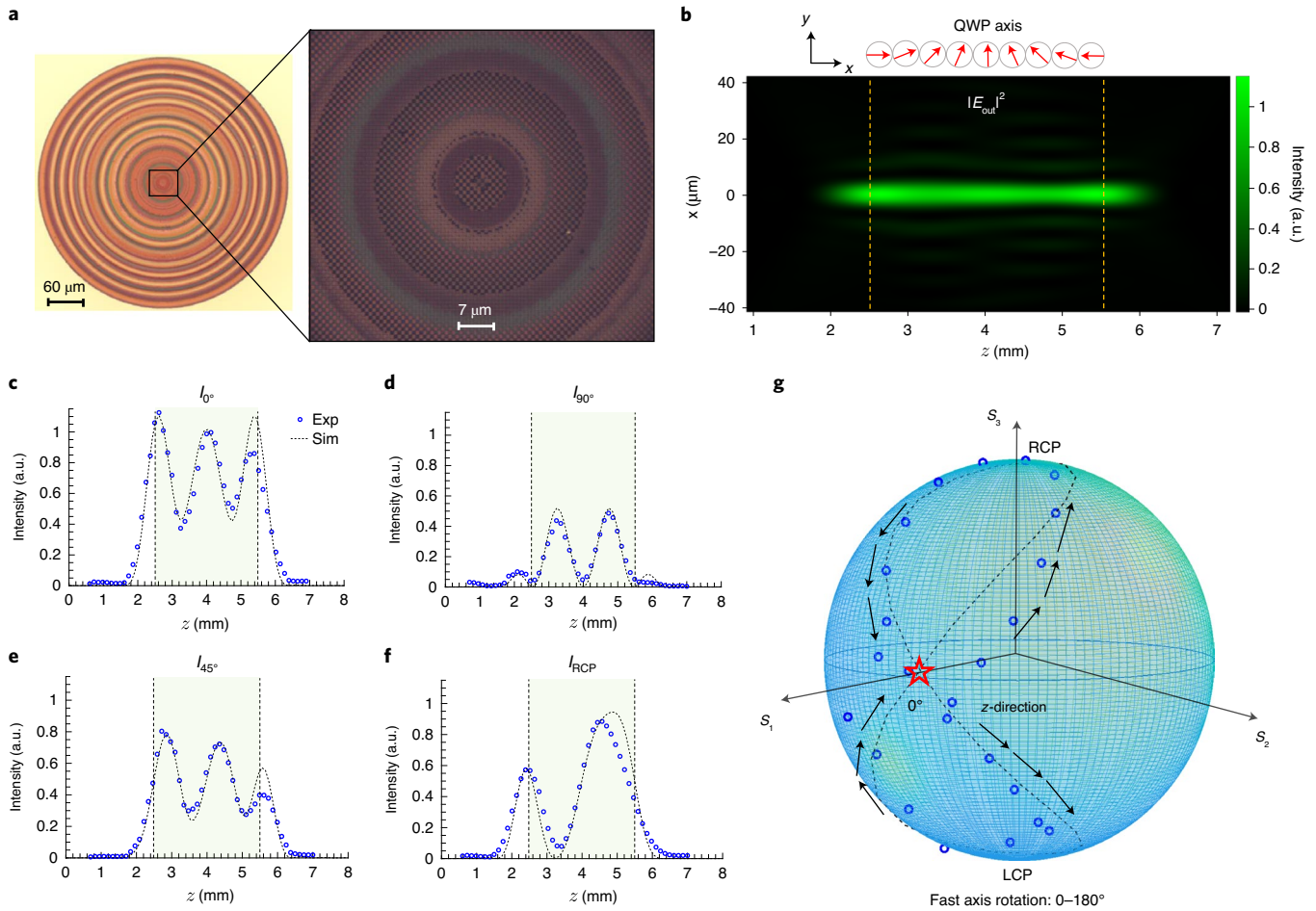

Fig. 5 | z-dependent QWP. a, Optical microscope images of the fabricated device. **b**, A simulated longitudinal intensity profile of the output beam under *x*-polarized illumination. The red arrows depict the virtual orientation of the fast axis of the device at different planes along *z*, whereas the vertical dashed lines mark the region of space over which the fast axis rotates from 0° to 180°. **c**–**e**, Measured and simulated on-axis intensity profiles as a function of *z* when the output analyser's axis is oriented at 0°(**c**), 90° (**d**) and 45° (**e**), without inserting the QWP before the CCD. **f**, Measured on-axis intensity profile as a function of *z* when the axes of the output QWP and analyser (before the CCD) are oriented at 0° and 45°, respectively, to analyse for RCP. **g**, The measured Stokes trajectory on the Poincare sphere with propagation along the *z*-direction under *x*-incident polarization.

QWP. Finally, to further show the versatility of this design approach, we now demonstrate a *z*-dependent QWP (shown in the optical micrograph of Fig. 5a). This device was designed to rotate its principal axis virtually in space by 180° within the region $z = 2.5$–5.5 mm and should thus modify the chirality (ellipticity) of an incident waveform. Figure 5b shows the longitudinal intensity profile of the output beam, assuming $\hat{x}$ incident polarization. The red arrows denote the orientation of the spatially rotating retarder axis over the region of interest bounded by the vertical lines.

We again carry out full Stokes polarimetry to test the behaviour of the device, the results of which are depicted in Fig. 5c–f. Here, the maxima of I_{0° (and minima of I_{90°) correspond to crossing the $(S_1 = 1, S_2 = 0, S_3 = 0)$ point on the Poincaré sphere (that is, *x*-polarization), whereas the minima of I_{0° (and maxima of I_{90°) correspond to traversing the south (0,0,−1) and north (0,0,1) poles, respectively. In essence, the south (0,0,−1) and north (0,0,1) poles of the Poincaré sphere map to the minimum and maximum points on the I_{RCP} curve, respectively.

The Stokes trajectory on the Poincaré sphere is shown in Fig. 5g as a function of *z* under $\hat{x}$ incident polarization. To interpret this result, recall that the action of a wave plate is represented by a precession of the Stokes vector on the Poincaré Sphere. The precession axis and its path on the latter is determined by the angular orientation and the retardance of the wave plate, respectively. The action of this QWP can be visualized as a precession along the path intersecting the Poincaré sphere and a cylinder centered about (0.5,0,0) where the output polarization state traverses a closed-looped trajectory in which it evolves from linear polarization to elliptical then becomes LCP before it gradually loses its ellipticity, retaining its original linear polarization. This behaviour is analogously repeated in the northern hemisphere. The outer rings of the beam play a critical role in achieving this propagation-dependent polarization transformation and spin state conversion. Essentially, these outer rings act as a reservoir that account for the spin angular momentum deficit ensuring that the target polarization response is enacted on the non-diffracting centre spot of the beam without violating any conservation laws. This occurs via a deliberate exchange of energy and momentum across different regions of the beam allowing the polarization state to change only locally without disturbing the global spin angular momentum, as detailed in Supplementary Section 5.

Discussion and outlook

We demonstrated how metasurfaces can enact longitudinally varying polarization behaviour. Previous work of this nature using digital holography often attempted to engineer the Jones vector of the output waveform under the assumption (constraint) of fixed input

polarization. On the contrary, our Jones matrix design approach decouples the target output response from the input polarization, allowing full control over the transfer function of the polarizing device and enabling its operation on all incident polarizations at once. This has been demonstrated in Fig. 3 where the intended polarizing action was enacted on each incident polarization, and in Fig. 4h–j where polarization rotation was observed regardless of the input polarization (and without introducing any modification to the set-up). Replicating this behaviour using digital holography would mandate the use of at least three SLMs, as illustrated in Supplementary Section 4. These SLM configurations, although appealing from the programmability point of view, rely on multiple active components in separate planes, which must be precisely aligned and imaged onto one another; this configuration cannot be afforded in many applications. By contrast, our work presents versatile polarization control using a single, integrated device. It also provides a previously unattained degree of polarization tunability from a static metasurface. In the future, methods of this nature could be combined with active metasurface platforms to attain even more versatile control.

It is noteworthy that although polarizing elements were designed at 532 nm, with a diameter of 462 μm, our approach applies to other wavelengths with adjustable scales for the transverse and longitudinal dimensions, as detailed in Supplementary Section 6. Furthermore, our design strategy permits sophisticated polarizing elements that can simultaneously realize diattenuation and retardance. For example, the polarizing metasurface can be designed to act as an analyser over one region of space and a retarder over another. Furthermore, our approach can be extended to create spin–orbit-mediated structured light and optical vortices with on-demand transverse profiles[50] by allowing equation (1) to admit higher-order Bessel functions. One area of improvement is to extend the scalar formulation in equation (1) to the full vectorial case to account for all three field components. This will relax the paraxiality condition in the design and enable optical elements that operate in the subwavelength regime, thus offering three-dimensional polarization control.

Several applications can benefit from these new polarization optics. The polarization-tunable axicon depicted in Fig. 3l may find application in optical trapping where a microparticle can be pushed or pulled along the optical path by changing the input polarization. It can also be used to spatially tailor the excitation of optically pumped media[35]. Moreover, if illuminated by a partially polarized beam, these devices can change the degree of polarization of output light with propagation. Furthermore, structured light with varying polarization may suggest new schemes in sensing as polarization rotation is a function of the optical length. Hence, by shining polarized light from our z-dependent HWP through a medium, the angle by which polarization is rotated can directly identify the unknown refractive index of the medium, as fully detailed in Supplementary Section 9. These devices can also be utilized to spatially modulate the spectrum of quantum emitters[37], to control the shape and size of laser-machined structures [23], and to enhance optical chirality in light–matter interaction[36], therefore opening many new paths.

Online content

Any methods, additional references, Nature Research reporting summaries, source data, extended data, supplementary information, acknowledgements, peer review information; details of author contributions and competing interests; and statements of data and code availability are available at https://doi.org/10.1038/s41566-020-00750-2.

Received: 22 May 2020; Accepted: 7 December 2020;
Published online: 28 January 2021

References

1. Goldstein, D. H. & Collett, E. *Polarized Light 3* (Taylor and Francis, 2003).
2. Scully, M. O. & Zubairy, M. S. Quantum optics. *Am. J. Phys.* **67**, 648–648 (1999).
3. Demos, S. G. & Alfano, R. R. Optical polarization imaging. *Appl. Opt.* **36**, 150–155 (1997).
4. Holliman, N. S., Dodgson, N. A., Favalora, G. E. & Pockett, L. Three-dimensional displays: a review and applications analysis. *IEEE Trans. Broadcast.* **57**, 362–371 (2011).
5. Tyo, J. S., Goldstein, D. L., Chenault, D. B. & Shaw, J. A. Review of passive imaging polarimetry for remote sensing applications. *Appl. Opt.* **45**, 5453–5469 (2006).
6. Bomzon, Z., Biener, G., Kleiner, V. & Hasman, E. Space-variant pancharatnam–berry phase optical elements with computer-generated subwavelength gratings. *Opt. Lett.* **27**, 1141–1143 (2002).
7. Yin, X., Ye, Z., Rho, J., Wang, Y. & Zhang, X. Photonic spin hall effect at metasurfaces. *Science* **339**, 1405–1407 (2013).
8. Ling, X. et al. Giant photonic spin hall effect in momentum space in a structured metamaterial with spatially varying birefringence. *Light Sci. Appl.* **4**, e290 (2015).
9. Balthasar Mueller, J. P., Rubin, N. A., Devlin, R. C., Groever, B. & Capasso, F. Metasurface polarization optics: independent phase control of arbitrary orthogonal states of polarization. *Phys. Rev. Lett.* **118**, 113901 (2017).
10. Arbabi, A., Horie, Y., Bagheri, M. & Faraon, A. Dielectric metasurfaces for complete control of phase and polarization with subwavelength spatial resolution and high transmission. *Nat. Nanotechnol.* **10**, 937–943 (2015).
11. Kruk, S. et al. Invited article: broadband highly efficient dielectric metadevices for polarization control. *APL Photon.* **1**, 030801 (2016).
12. Shi, Z. et al. Continuous angle-tunable birefringence with freeform metasurfaces for arbitrary polarization conversion. *Sci. Adv.* **6**, eaba3367 (2020).
13. Intaravanne, Y. & Chen, X. Recent advances in optical metasurfaces for polarization detection and engineered polarization profiles. *Nanophotonics* **9**, 0479 (2020).
14. Davis, J. A. et al. Diffraction gratings generating orders with selective states of polarization. *Opt. Express* **24**, 907–917 (2016).
15. Rubin, N. A. et al. Polarization state generation and measurement with a single metasurface. *Opt. Express* **26**, 21455–21478 (2018).
16. Deng, Z.-L. et al. Diatomic metasurface for vectorial holography. *Nano Lett.* **18**, 2885–2892 (2018).
17. Rubin, N. A. et al. Matrix fourier optics enables a compact full-stokes polarization camera. *Science* **365**, eaax1839 (2019).
18. Pfeiffer, C. & Grbic, A. Controlling vector bessel beams with metasurfaces. *Phys. Rev. Applied* **2**, 044012 (2014).
19. Zhan, Q. Cylindrical vector beams: from mathematical concepts to applications. *Adv. Opt. Photon.* **1**, 1–57 (2009).
20. Naidoo, D. et al. Controlled generation of higher-order poincaré sphere beams from a laser. *Nat. Photon.* **10**, 327–332 (2016).
21. Nieminen, T. A., Heckenberg, N. R. & Rubinsztein-Dunlop, H. Forces in optical tweezers with radially and azimuthally polarized trapping beams. *Opt. Lett.* **33**, 122–124 (2008).
22. Shvedov, V., Davoyan, A. R., Hnatovsky, C., Engheta, N. & Krolikowski, W. A long-range polarization-controlled optical tractor beam. *Nat. Photon.* **8**, 846–850 (2014).
23. Hnatovsky, C., Shvedov, V. G., Shostka, N., Rode, A. V. & Krolikowski, W. Polarization-dependent ablation of silicon using tightly focused femtosecond laser vortex pulses. *Opt. Lett.* **37**, 226–228 (2012).
24. Milione, G., Nguyen, T. A., Leach, J., Nolan, D. A. & Alfano, R. R. Using the nonseparability of vector beams to encode information for optical communication. *Opt. Lett.* **40**, 4887–4890 (2015).
25. Xie, X., Chen, Y., Yang, K. & Zhou, J. Harnessing the point-spread function for high-resolution far-field optical microscopy. *Phys. Rev. Lett.* **113**, 263901 (2014).
26. Bryant, D. M. & Mostov, K. E. From cells to organs: building polarized tissue. *Nat. Rev. Mol. Cell Biol.* **9**, 887–901 (2008).
27. Moreno, I., Davis, J. A., Sánchez-López, M. M., Badham, K. & Cottrell, D. M. Nondiffracting bessel beams with polarization state that varies with propagation distance. *Opt. Lett.* **40**, 5451–5454 (2015).
28. Fu, S., Zhang, S. & Gao, C. Bessel beams with spatial oscillating polarization. *Sci. Rep.* **6**, 30765(2016).
29. Li, P. et al. Generation and self-healing of vector bessel-gauss beams with variant state of polarizations upon propagation. *Opt. Express* **25**, 5821–5831 (2017).
30. Chen, R.-P., Chen, Z., Gao, Y., Ding, J. & He, S. Flexible manipulation of the polarization conversions in a structured vector field in free space. *Laser Photon. Rev.* **11**, 1700165 (2017).
31. Corato-Zanarella, M., Dorrah, A. H., Zamboni-Rached, M. & Mojahedi, M. Arbitrary control of polarization and intensity profiles of diffraction-attenuation-resistant beams along the propagation direction. *Phys. Rev. Appl.* **9**, 024013 (2018).

32. Otte, E., Rosales-Guzmán, C., Ndagano, B., Denz, C. & Forbes, A. Entanglement beating in free space through spin–orbit coupling. *Light Sci. Appl.* **7**, 18009 (2018).
33. Li, P. et al. Three-dimensional modulations on the states of polarization of light fields. *Chin. Phys. B* **27**, 114201 (2018).
34. Hu, Q., Dai, Y., He, C. & Booth, M. J. Arbitrary vectorial state conversion using liquid crystal spatial light modulators. *Opt. Commun.* **459**, 125028 (2020).
35. Fatemi, F. K. Cylindrical vector beams for rapid polarization-dependent measurements in atomic systems. *Opt. Express* **19**, 25143–25150 (2011).
36. Tang, Y. & Cohen, A. E. Optical chirality and its interaction with matter. *Phys. Rev. Lett.* **104**, 163901 (2010).
37. Santhosh, K., Bitton, O., Chuntonov, L. & Haran, G. Vacuum Rabi splitting in a plasmonic cavity at the single quantum emitter limit. *Nat. Commun.* **7**, 11823 (2016).
38. Jones, R. C. A new calculus for the treatment of optical systems. I. Description and discussion of the calculus. *J. Opt. Soc. Am.* **31**, 488–493 (1941).
39. Durnin, J. Exact solutions for nondiffracting beams. I. The scalar theory. *J. Opt. Soc. Am. A* **4**, 651–654 (1987).
40. McGloin, D. & Dholakia, K. Bessel beams: diffraction in a new light. *Contemporary Phys.* **46**, 15–28 (2005).
41. Goodman, J. *Introduction to Fourier Optics* (W. H. Freeman, 2005).
42. Zamboni-Rached, M. Stationary optical wave fields with arbitrary longitudinal shape by superposing equal frequency bessel beams: frozen waves. *Optics Express* **12**, 4001–4006 (2004).
43. Yu, N. & Capasso, F. Flat optics with designer metasurfaces. *Nat. Mater.* **13**, 139–150 (2014).
44. Devlin, R. C., Khorasaninejad, M., Chen, W. T., Oh, J. & Capasso, F. Broadband high-efficiency dielectric metasurfaces for the visible spectrum. *Proc. Natl Acad. Sci. USA* **113**, 10473–10478 (2016).
45. Berry, M. V. Quantal phase factors accompanying adiabatic changes. *Proc. R. Soc. Lond. A* **392**, 45–57 (1984).
46. Zhu, A. Y. et al. Giant intrinsic chiro-optical activity in planar dielectric nanostructures. *Light Sci. Appl.* **7**, 17158–17158 (2018).
47. Fienup, J. R. Phase retrieval algorithms: a comparison. *Appl. Opt.* **21**, 2758–2769 (1982).
48. Hsueh, C. K. & Sawchuk, A. A. Computer-generated double-phase holograms. *Appl. Opt.* **17**, 3874–3883 (1978).
49. Mendoza-Yero, O., Mínguez-Vega, G. & Lancis, J. Encoding complex fields by using a phase-only optical element. *Opt. Lett.* **39**, 1740–1743 (2014).
50. Aleksanyan, A. & Brasselet, E. Spin–orbit photonic interaction engineering of bessel beams. *Optica* **3**, 167–174 (2016).

Methods

Constructing the desired *z*-dependent Jones matrix function. The formalism given by equation (2) in the main text permits any z-dependent Jones matrix function $\tilde{F}(z)$; however, here we focus on perhaps the most fundamental polarizing element: a linear polarizer. As an example, we construct an $\tilde{F}(z)$ describing a linear polarizer whose principal axis rotates with z. A linear polarizer whose principal axis is aligned with the x-axis is represented in the Cartesian coordinates by the Jones matrix $\tilde{J}_{\mathrm{LP}} = [1\ 0]^T[1\ 0]$. More generally, a linear polarizer that is rotated by an angle ϕ with respect to the x-axis is described as $R(-\phi)\tilde{J}_{\mathrm{LP}}R(\phi)$, where $R(\phi)$ is the 2×2 rotational matrix. In our desired device, the polarizer's rotation varies with z in accordance with a desired function $\phi(z)$ so that its Jones matrix is given by

$$\tilde{J}_{\mathrm{LP}}(z) = \begin{bmatrix} \cos^2(\phi_z) & \cos(\phi_z)\sin(\phi_z) \\ \cos(\phi_z)\sin(\phi_z) & \sin^2(\phi_z) \end{bmatrix}. \tag{4}$$

Here we have denoted $\phi(z)$ as ϕ_z for clarity. Similarly, the Jones matrix of a wave plate with a z-dependent rotation is given by

$$\tilde{J}_{\mathrm{WP}}(z) = \begin{bmatrix} \cos(\theta/2) + i\sin(\theta/2)\cos(2\phi_z) & i\sin(\theta/2)\sin(2\phi_z) \\ i\sin(\theta/2)\sin(2\phi_z) & \cos(\theta/2) - i\sin(\theta/2)\cos(2\phi_z) \end{bmatrix}, \tag{5}$$

where θ denotes the retardance, that is, relative phase shift between the eigen vectors of the wave plate (for example, $\theta=\pi, \pi/2$ for a HWP and QWP, respectively). By substituting equations (4) and (5) into equation (2) to calculate $\tilde{A}^{(m)}$, and then evaluating $\tilde{U}(r, z=0)$ from equation (1), one can obtain the 2×2 Jones matrix distribution that forms the variable polarizer.

Dual matrix holography. We expanded on the scalar technique of dual-phase holography introduced in ref. [49] to perform complex modulation using phase-only platforms, to apply to Jones matrices. More specifically, we developed a dual matrix holography technique that enabled the realization of complex 2×2 matrices (that are non-unitary in general) using unitary platforms. Our approach was essentially to express an arbitrary matrix (with complex eigenvalues) as a summation of two unitary matrices whose eigenvalues are phase quantities, a matrix generalization of scalar dual-phase holography. To transform our target distribution of spatially varying 2×2 complex Jones matrices into a unitary only distribution, we ran the following procedure:

(1) The desired matrix distribution $\tilde{U}(r, z=0)$ is first obtained by evaluating equation (1).

(2) $\tilde{U}(r, z=0)$ is then normalized, locally, by dividing by the global maximum eigen value: $\tilde{u}(r, z=0) = \frac{\tilde{U}(r,z=0)}{\max\{\mathrm{eig}(\tilde{U})\}}, \forall r$. In practice, this normalization step is required as our passive metasurface may only introduce a loss-like effect in the Fourier plane with no gain.

(3) At each location in the transverse plane, $\tilde{u}(r, z=0)$ decomposes into two unitary matrices by means of singular value decomposition. This decomposition serves as a factorization for each 2×2 normalized Jones matrix such that $\tilde{u} = [WDV^T]$, where D is now a 2×2 diagonal matrix with non-negative real singular values.

(4) The singular values of $\tilde{u}$, D_{11} and D_{22}, at each location, decompose into a sum of two complex values $C_{ii}^{(1)} = (D_{ii} + i\sqrt{1-D_{ii}^2})/2$ and $C_{ii}^{(2)} = (D_{ii} - i\sqrt{1-D_{ii}^2})/2$, where i denotes the index of the diagonal entry (ii=11 or 22). Here the spatial dependence on r has been omitted for clarity.

(5) The complex values $C_{ii}^{(1,2)}$ then become the new diagonal entries of two unitary matrices, with the same rotation matrices W and V^T, such that

$$\tilde{u}(r, z=0) = \tilde{u}_1 + \tilde{u}_2 = W\begin{bmatrix} C_{11}^{(1)}(r) & 0 \\ 0 & C_{22}^{(1)}(r) \end{bmatrix}V^T + W\begin{bmatrix} C_{11}^{(2)}(r) & 0 \\ 0 & C_{22}^{(2)}(r) \end{bmatrix}V^T. \tag{6}$$

By construction, $D_{ii} = C_{ii}^{(1)} + C_{ii}^{(2)}$ and $|C_{ii}^{(1,2)}| = 1, \forall r$. As such, $\tilde{u}(r, z=0)$ decomposes into two unitary matrices, denoted $\tilde{u}_1$ and $\tilde{u}_2$, where each can be implemented using our proposed (unitary) dielectric metasurface comprised of wave-plate-like unit cells. Through judicious interlacing of $\tilde{u}_1$ and $\tilde{u}_2$ on the same metasurface, the intended polarization behaviour of the device can be achieved at the far field. To achieve this, $\tilde{u}_1$ and $\tilde{u}_2$ were periodically sampled by means of two complementary draughts board patterns, M_1 and M_2, expressed as

$$M_{1,2}(r,\phi) = \frac{1}{2}\sum_{n=-\infty}^{\infty}\sum_{l=-\infty}^{\infty}\mathbb{I}[\Lambda_{1,2}(n,l)]e^{\frac{i2\pi r}{p}(n\cos\phi + l\sin\phi)}, \tag{7}$$

$$\Lambda_{1,2}(n,l) = \cos\left[\frac{\pi(n\pm l)}{2}\right]\mathrm{sinc}\left(\frac{n\pi}{2}\right)\mathrm{sinc}\left(\frac{l\pi}{2}\right). \tag{8}$$

Here, p defines the periodicity of the draughts board pattern. In essence, equation (7) renders two complementary draughts board patterns whose transverse profile at each location alternates between $\mathbb{I}$ and the zero matrix. Multiplying $\tilde{u}_{1,2}$ by $M_{1,2}$, locally, and adding becomes equivalent to interlacing $\tilde{u}_1$ and $\tilde{u}_2$ onto the same surface with a period of p. Notably, allowing p to fulfil the Nyquist limit enables the full reconstruction of the transfer function of $\tilde{u}(r, z=0)$ in the far field [49]. The interlaced pattern at the metasurface plane is given by

$$\tilde{\mathcal{I}}(r,\phi) = M_1(r,\phi)\tilde{u}_1(r) + M_2(r,\phi)\tilde{u}_2(r). \tag{9}$$

By taking the Fourier transform of the matrix $\tilde{\mathcal{I}}(r,\phi)$, it can be shown that $\mathcal{F}\{\tilde{\mathcal{I}}(r,\phi)\} = \tilde{H}_1(u,v) + \tilde{H}_2(u,v)$, where

$$\tilde{H}_1(u,v) = \sum_{n=-\infty}^{\infty}\sum_{l=-\infty}^{\infty}\Lambda_1(n,l)\tilde{\mathbf{\Psi}}(u-\frac{n}{p}, v-\frac{l}{p}), \tag{10}$$

and,

$$\tilde{H}_2(u,v) = \sum_{n=-\infty}^{\infty}\sum_{l=-\infty}^{\infty}\Lambda_2(n,l)\tilde{\mathbf{\Omega}}(u-\frac{n}{p}, v-\frac{l}{p}). \tag{11}$$

Here, $\tilde{\mathbf{\Psi}} = \mathcal{F}\{\tilde{u}_1(r)\}$ and $\tilde{\mathbf{\Omega}} = \mathcal{F}\{\tilde{u}_2(r)\}$. In essence, $\mathcal{F}\{\tilde{\mathcal{I}}(r,\phi)\}$ yields multiple copies of the spectra $\tilde{\mathbf{\Psi}}$ and $\tilde{\mathbf{\Omega}}$, about the points $(\frac{n}{p}, \frac{l}{p})$. As $\tilde{U}(r, z=0)$ is band-limited, from the definition of equation (1), then its true complex spectrum $[\tilde{\mathbf{\Psi}}(u,v) + \tilde{\mathbf{\Omega}}(u,v)]$ can be fully reconstructed by filtering in the k-space provided that the p satisfies the Nyquist criteria (that is, $\frac{1}{p} \geq \frac{\max(k_r^{(m)})}{2}$). As $\tilde{U}(r, z=0) = \tilde{u}_1(r) + \tilde{u}_2(r)$, it follows that $\mathcal{F}\{\tilde{U}(r, z=0)\} = \tilde{\mathbf{\Psi}}(u,v) + \tilde{\mathbf{\Omega}}(u,v)$ and so the desired spectrum is fully reconstructed. The original matrix $\tilde{U}(r, z=0)$ can then be retrieved by performing an inverse Fourier operation.

Metasurface design and fabrication. In our designs, we set $N=5$ for the analyser and $N=7$ for the wave plates, where $2N+1$ defines the number of Bessel functions implemented by the device as per equation (1). We also set the central spatial frequency $k_z^{(0)}$ at a value of $0.9995\,\omega/c$ with a separation of $2\pi/L$ in k-space, where $L=10$ mm. This choice of N and the wavevectors ensures operation in the paraxial regime where the scalar formulation given in equation (1) holds and the contribution of the longitudinal field component can be neglected. All devices have a diameter of 462 μm, which was chosen to ensure beam propagation over the range defined by L, verified from Kirchhoff diffraction calculations. Note that longer beam control ranges can be achieved by increasing the aperture size of the device. The precise relationship between the aperture size and the beam's range can be derived from a geometric argument that pertains to axicons, as detailed in Supplementary Section 6. This argument applies to our devices as they generate diffraction-resistant Bessel-like beams.

To create the metasurface profile, a library of unit cells comprised of rectangular dielectric nanopillars of high refractive index (TiO_2) has been constructed by varying the pillar dimensions (d_x and d_y) and their angular orientation. This was performed at $\lambda=532$ nm using a finite-difference time-domain simulation under plane-wave illumination, periodic boundary conditions, unit cell separation of 420 nm and fixed pillar height of 600 nm. As such, we constructed a library of structures that can realize the Jones matrix of equation (3) within the domain $\theta_{x,y}=[0, 2\pi]$ and $\phi=[0, \pi]$, with almost uniform transmission and high efficiency (~75%). Each transverse location on the metasurface is realized by selecting its closest pillar geometry from our library, as further detailed in Supplementary Section 3.

All devices have been fabricated using a process reliant on electron beam lithography and atomic layer deposition, as described in ref. [44]. The procedure is as follows: a fused silica substrate is spin-coated with a positive tone electron beam resist that ultimately defines the height of the nanopillars. After baking the resist, the desired pillar patterns were written by exposing the resist using electron beam lithography (with an accelerating voltage of 125 kV), then developed in o-xylene for 60 s. The developed pattern now defines the geometry of the individual nanopillars. Afterwards, TiO_2 was deposited via atomic layer deposition process to conformally fill the developed pattern. The excess layer of TiO_2 on top of the device was etched away using reactive ion etching to the original height of the resist. Finally, the resist was chemically removed away leaving the individual TiO_2 nanopillars surrounded by air.

Experimental set-up. The polarizing metasurfaces were tested using the set-up of Fig. 2c. First, a $\lambda=532$ nm laser beam was spatially filtered through a 100 μm pinhole and collimated using a 10 cm lens to provide a quasi-plane-wave illumination on the metasurface. A polarizer and HWP rotate the incident polarization so that the metasurface behaviour can be measured in response to different polarization states. A 4f system, comprising two lenses ($f=5$ cm), was used to filter and image the response of the metasurface onto a CCD camera. Lens 1 performs the Fourier operation required to retrieve the complex (amplitude and phase) spectrum of the signal in k-space, thereby achieving step 4 of Fig. 2a. The generated Fourier spectrum (at the focal plane of lens 1) was filtered in k-space from higher diffraction orders before it was transformed back to real space via an inverse Fourier operation performed by lens 2, as outlined in step 5 of Fig. 2a. Due to their large diffraction angle, these higher orders were naturally filtered away

by escaping the aperture of lens 2 (2.54 cm diameter). The output beam with its desired polarization behaviour was then recorded using a CCD camera that was mounted on a translational stage to sample along the z-direction, where $z=0$ plane lies at the output focal plane of lens 2. To characterize the polarization behaviour of the output beam at each z-plane, we performed polarization measurements based on Stokes polarimetry. This enabled the determination of the full, four-component polarization Stokes vector, $\mathbf{S} = (S_0, S_1, S_2, S_3)^T$, which quantified the shape and orientation of the polarization ellipse at each point as well as the beam's intensity and degree of polarization. The Stokes parameters were obtained by rotating a polarizer and a QWP before the CCD to analyse for four different polarization states: 0°, 45°, 90° and RCP.

Data availability

All key data generated and analysed are included in this paper and its Supplementary Information. Additional datasets that support the plots within this paper and other findings of this study are available from the corresponding author on reasonable request.

Code availability

The codes and simulation files that support the plots and data analysis within this paper are available from the corresponding author on reasonable request.

Acknowledgements

We thank W.-T. Chen and X. Yin, both of Harvard University, for their helpful discussions. A.H.D. acknowledges the financial support from the Natural Sciences and Engineering Research Council of Canada (NSERC) under grant no. PDF-533013-2019. N.A.R. acknowledges support from the National Science Foundation Graduate Research Fellowship Program (GRFP) under grant no. DGE1144152. This work was performed in part at the Center for Nanoscale Systems (CNS), a member of the National Nanotechnology Coordinated Infrastructure (NNCI), which is supported by the National Science Foundation under NSF award no. 1541959. CNS is part of Harvard University. Additionally, financial support from the Office of Naval Research (ONR) MURI program, under grant no. N00014-20-1-2450, and from the Air Force Office of Scientific Research (AFOSR), grant no. FA95550-19-1-0135, is acknowledged.

Author contributions

A.H.D. and N.A.R. developed the theoretical framework and fabricated the devices. A.Z. helped formulate the dual matrix holography theory. A.H.D. designed and measured the devices and analysed the data. M.T. contributed to the fabrication and characterization of the devices. A.H.D., N.A.R. and F.C. wrote the manuscript. F.C. supervised the project.

Competing interests

The authors declare no competing interests.

Additional information

Supplementary information is available for this paper at https://doi.org/10.1038/s41566-020-00750-2.

Correspondence and requests for materials should be addressed to F.C.

Nature Photonics thanks Philippe St-Jean and the other, anonymous, reviewer(s) for their contribution to the peer review of this work.

Reprints and permissions information is available at www.nature.com/reprints.